POLITECNICO DI TORINO
Repository ISTITUZIONALE

Active and Selective Ensembles in Oxide-Derived Copper Catalysts for CO2 Reduction

(Article begins on next page)

07 August 2024

Active and Selective Ensembles in Oxide-Derived Copper Catalysts for CO2 Reduction

Federico Dattila, Rodrigo García-Muelas, and Núria López*

Read Online

ACCESS | Metrics & More | Article Recommendations | Supporting Information

ABSTRACT: Copper catalysts are unique in CO_2 reduction as they allow the formation of C_{2+} products. Depending on the catalysts' synthesis, product distribution varies significantly: while Cu nanoparticles produce mainly methane and hydrogen, oxide-derived copper leads to ethylene and ethanol. Here, by means of *ab initio* molecular dynamics on oxygen-depleted models, we identified the ensembles controlling catalytic performance. Upon reconstruction and irrespective of the starting structure, recurrent patterns defined by their coordination and charges appear: metallic Cu^0, polarized $Cu^{\delta+}$, and oxidic Cu^+. These species combine to form 14 ensembles. Among them, 4-(6-)coordinated Cu adatoms and $Cu_3^{\delta+}O_3$ are responsible for tethering CO_2, while metastable near-surface oxygens in fcc-(111) or (100)-like Cu domains promote C−C bond formation via glyoxylate species, thus triggering selective C_{2+} production at low onset potentials. Our work provides guidelines for modeling complex structural rearrangements under CO_2 reduction conditions and devising new synthetic protocols toward an enhanced catalytic performance.
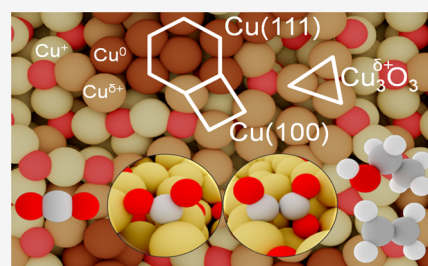
C O_2 reduction (CO_2R) has emerged as a suitable way to store renewable energy as chemical bonds.[1−3] Copper has a unique ability to promote C−C coupling toward C_{2+} products,[4] which are among the most sought-after chemicals.[5] Under reaction conditions, most copper-based catalysts reconstruct because of reaction intermediates and surface polarization caused by the applied electric potential.[6−9] As a consequence, the sample's history affects the activity, selectivity, and stability of the catalyst[6,10,11] (Table S1). In particular, polycrystalline Cu generates mainly CO, HCOOH, $HCOO^-$, H_2, and CH_4 at potentials more reductive than −0.8 V vs RHE,[12−15] while (110) and (111) steps nearby (100) terraces are selective toward C_{2+} products.[12] Instead, oxide-derived Cu catalysts (OD-Cu) show a higher overall activity for producing ethylene,[15−23] ethanol,[17] n-propanol,[17,24] n-butanol,[25] and traces of acetate and ethane,[17,26] at lower overpotentials than copper nanoparticles.[14,27−29]

To understand and control the key properties of OD-Cu upon reconstruction is crucial to rationally design more active and selective catalysts. It is generally thought that reconstruction boosts activity by increasing the electrochemically active surface area.[2,7,20,30] Regarding selectivity, CO dimerization is considered the crucial selectivity switch toward C_{2+} products.[2,31,32] Several features have been deemed responsible to promote that step, such as low coordinated Cu sites,[11,14,18,33] grain boundaries,[6,17,34] defects,[6,7] open facets,[6,27,35] surface roughness,[7,20] high surface pH,[35−37] cation effects,[2,32] and polarized $Cu^{\delta+}$ sites induced by residual oxygen.[6,15,20,22,23,38,39]

However, the specific ensembles which control the selectivity to each product have not yet been identified.

The existence of residual oxygen on OD-Cu catalysts has been strongly debated in the literature, as its presence depends on the history of the material. Thermodynamically, copper oxide is expected to get fully reduced at neutral and alkaline pH for electric potentials lower than −0.1 V vs RHE (Figure S1). However, near-surface oxygen can be trapped kinetically[40] by oxidizing deeply the Cu sample before reduction[41] and by applying high cathodic potentials immediately after oxidation.[23,42] Near-surface oxygen atoms can also be restored by applying pulsed electrolysis[6,30] and by including a co-oxidant.[43] In contrast, materials obtained by shallow air oxidization of mono- or polycrystalline Cu get reduced beyond oxygen detection limits at CO_2 reduction conditions.[44,45] Preoxidation of polycrystalline Cu by mild anodic potentials also results in a low concentration of oxygen sites.[28] When present, residual oxygen atoms do not belong to bulk phases of copper oxide[46] but rather prefer grain boundaries[28] where Cu atoms have an oxidation state intermediate between Cu^0 and Cu^+.[30,39,47] Both residual oxygen and grain boundaries promote C_{2+} products.[34,39] Density functional theory (DFT) models have found
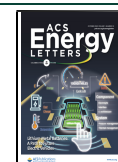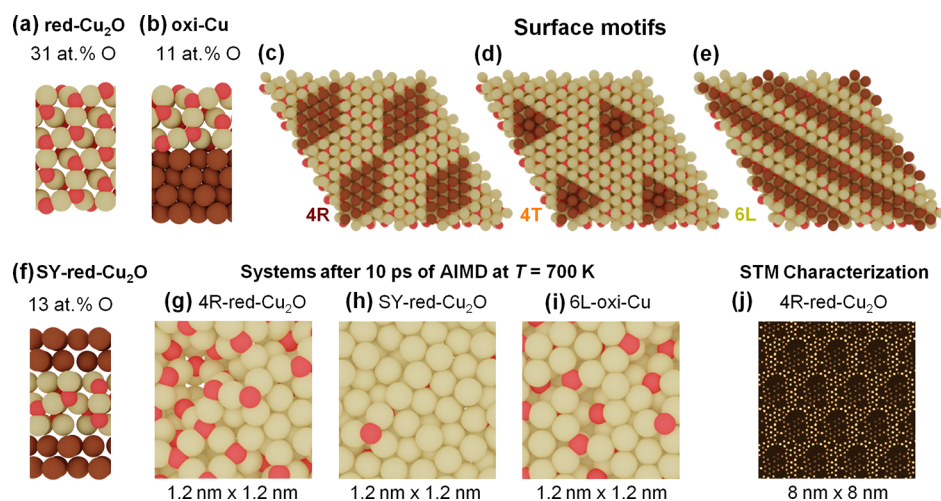
Figure 1. Models for OD-Cu. We considered two systems: (a) a $Cu_2O(111)$ slab to mimic Cu_2O reduction (red-Cu_2O) and (b) a Cu(111)/Cu_2O configuration to resemble Cu oxidation (oxi-Cu) (side views). For each supercell, O atoms were partially removed from the two outermost layers to create three depletion motifs: (c) rhomboidal (4R, patch), (d) triangular (4T, pitting), and (e) linear (6L, strip) (top views). (f) A symmetrical, Cu-terminated system (SY-red-Cu_2O) was included to investigate the influence of stoichiometry and depletion motifs. (g–i) After 10 ps of AIMD at 700 K, the final surfaces present analogous reconstruction (Videos S1–S7[55]) and (j) STM characterization detected similar patterns as experimental Cu/Cu_2O systems[56] (Figure S3). Red-Cu_2O and oxi-Cu systems were labeled nS, with n number of O atoms removed from the subsurface and S the shape of the O depleted region (dark brown). Red-Cu_2O and oxi-Cu suffixes were appended to differentiate both conditions.

that residual oxygen is stable and enhances CO adsorption in highly disordered structures,[48] but not at interstitial sites of crystalline Cu.[49,50] For crystalline phases, DFT simulations have rationalized the selectivities observed for (111), (100), and stepped Cu surfaces toward C_1–C_2 products as a function of CO and H energy descriptors.[3,51] Besides, linear scaling relationships between surface site reactivity and coordination numbers are commonly employed to assess the properties of metals and oxides, in particular for disordered environments.[52,53] However, theoretical models still need to be adapted to the dynamic view of catalytic interfaces, such as OD-Cu under CO_2 reduction conditions.[54]

As DFT-based modeling has focused on rather ideal structures, here we have envisaged an alternative way to understand the reactivity of OD-Cu. Starting from pristine oxides, we have removed oxygen atoms to create oxygen-depleted structures and allow reconstruction upon *ab initio* molecular dynamics. Although several crude approximations have been introduced (see below), we have identified new structural patterns that completely modify our understanding of these materials. In this way, we investigated roughness, coordination, oxidation states, and spectroscopic fingerprints for these structures, showing 14 recurrent ensembles with three chemical species: Cu^0, $Cu^{\delta+}$, and Cu^+. The ensembles characterized by mild polarization are responsible for OD-Cu enhanced activity and C_{2+} selectivity via a newly identified-glyoxylate-like intermediate, Table S2.

OD-Cu catalysts are typically synthesized via oxidation of Cu foils or by electrochemical reduction of copper oxides.[17,45] To mimic changes in OD-Cu morphology under reaction conditions, we built structural models to represent both reduction of Cu_2O (red-Cu_2O) and oxidation of Cu (oxi-Cu) (Figure 1a,b).

In the reduction models, OD-Cu were constructed as a $2\sqrt{3} \times 2\sqrt{3} - R30°$ $Cu_2O(111)$ supercell with about 21 Å lateral size. Then, the oxygens in the outermost layer (12/144) were removed, as suggested by ref 45, along with part of the

subsurface sites (4–6/144) to reproduce experimental reports (O content: 10–20 atom %).[19,20] The Cu/O stoichiometry for these systems accounted for an overall oxygen atomic percent of 31–30 atom %, higher than experimental values because of the contribution of the bulk oxide (Table S3). Oxygen depletion followed three different shapes: rhomboidal (R), triangular (T), and linear (L), to promote clustering, pitting, and formation of grain boundaries, respectively (Figures 1c–e and S2). The suboxide formation energies of these initial structures differ only by 0.01 eV/Cu atom (Table S3), proving that they are potentially equivalent starting points. The systems were labeled nS: n stands for the number of subsurface oxygens removed, and S indicates the depletion motif, R, L or T (Figure 1c–e). Deep reduction conditions were simulated through a symmetric slab (SY-red-Cu_2O), $2\sqrt{3} \times 2\sqrt{3} - R30°$ $Cu_2O(111)$ supercell, 7 layers thick. Here, just the two central Cu_2O layers were preserved while removing 120/168 of all the oxygen atoms, leaving 13 atom % of oxygen (Figure 1f). Alternatively, oxidized Cu surfaces were reproduced depositing three Cu_2O layers on $5\sqrt{3} \times 5\sqrt{3} - R30°$ bulk Cu(111) to recreate the geometric stress throughout surface reconstruction. Surface and subsurface oxygens were removed following the same procedure as before: taking the 4R model as reference, the formation energies by copper atom differ by ≤0.01 eV (0.21, 0.21, and 0.22 for the 4R, 4T, and 6L systems; Table S3).

Surface reconstruction was assessed through AIMD with the PBE density functional (ref 57) for 10 ps at 700 K (3 fs time step). Solvent, potential, and electrolyte were not included during AIMD simulations. Although the approximations of our models are severe, our analysis demonstrates the strong structural modifications which occur on these materials under reaction conditions. The assessment of the robustness of our results is summarized in Table S2. Benchmark tests on Hubbard correction and AIMD temperatures were performed on the 4R-red and 4R-oxi systems (Computational Methods in the Supporting Information). Similar surface patterns evolved
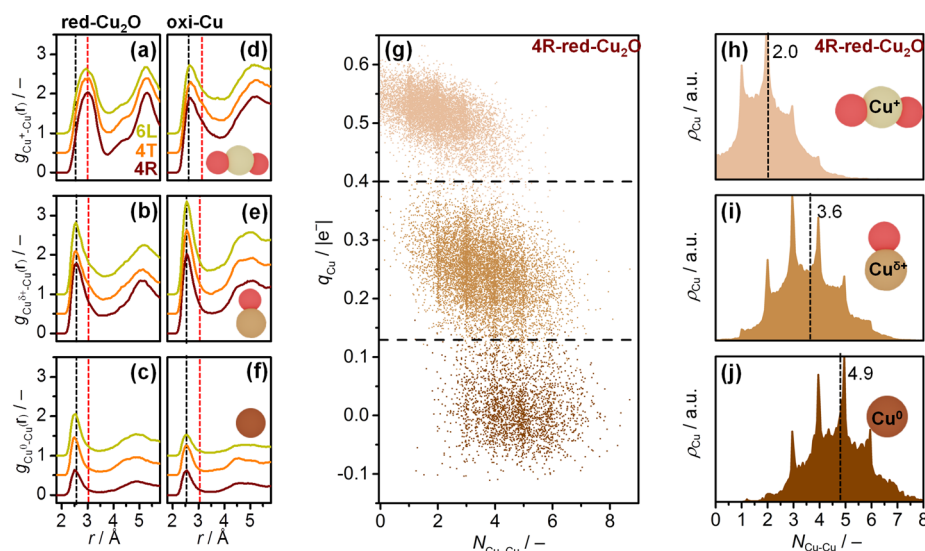
Figure 2. Characterization of Cu species. (a–f) Cu–Cu RDF for Cu atoms coordinated with 0–2 oxygens as shown in the insets. The first (second) coordination shell of bulk Cu (Cu$_2$O) is shown as black (red) dashed lines. Cu–Cu RDF for the SY-red-Cu$_2$O system is reported in Figure S12. (g) Cu atoms coordinated to 0–2 oxygens show clear differences in their Bader charges and number of Cu atoms in their first coordination shell. (h–j) Cu–Cu coordination number (N_{Cu-Cu}) cumulative maps show peaks at integer N_{Cu-Cu}, suggesting the existence of recurring ensembles. Average $\bar{N}_{Cu-Cu}$, dashed lines, differ by 1.0 units from metallic to polarized and almost 3.0 to oxidic Cu. Bader charges and N_{Cu-Cu} distributions for the remaining systems are reported in Figures S15 and S17.

upon reconstruction, while their abundance depended on Cu/O stoichiometry (Figure 1g–i). The final structures reproduced the overall disorder characterized by local recurrent features with around 1 nm periodicity and O depletion regions reported as dark areas in STM images of Cu$_2$O/Cu(111) surfaces under CO autocatalytic reduction[56] (Figure S3). The thermodynamic stability of the models was estimated from their Pourbaix diagrams. The final snapshots of the AIMD simulations were further optimized to their lowest-energy configuration, and solvation contributions were included to the optimized structures through an implicit model.[58,59] Stabilized by configurational entropy and solvation, our disordered systems are metastable.[60] Their formation energy is slightly higher than the thermodynamically stable phase (Cu$_2$O) by at most 0.1 eV, but significantly, they are more stable than experimentally reported oxidic phases, Cu$_8$O and Cu$_{64}$O[61] (Tables S4–S7, Figure S1, and eqs S5–S9). Moreover, in our models, O stability on reconstructed surfaces depends on its local coordination: at mild negative potential O desorption is endothermic because of high surface pH,[35–37,62] which may increase up to 14 for high cathodic current densities[63] (Supporting Discussion, Figure S4). Depending on the surface pH, the stability region of residual oxygens extends until −0.84 V vs RHE, in good agreement with recent experimental reports.[6,23,42,64,65] Uncertainty in surface pH determination by 1–2 units and the lack of configuration entropy contribution set the limit for O borderline-stability between −0.6 and −1.0 V vs RHE (Supporting Discussion). Structural characterization was performed on the two outermost layers for the whole AIMD production period. We investigated surface roughness (σ), number of surface sites, radial distribution functions (RDF), Cu coordination numbers (N_{Cu-Cu}), spectroscopic properties, and recurrent ensembles for each of the trajectories (Computational Methods). Final AIMD trajectories show similar Cu 2p and O 1s XPS fingerprints as OD-Cu experimental systems (Figure S5). Analogously, vibrational spectra (eqs S10–S13) qualitatively reproduce Raman shifts

detected in experimental reports, as shown in Figures S6 and S7.

OD-Cu activity has been attributed to a higher surface area upon reconstruction.[2,7,20,30] However, previous theoretical simulations did not succeed in quantifying nanostructuring.[39,46,48–51] Through the continuous reorganization induced by AIMD, we were able to assess OD-Cu reconstruction through arithmetic average surface roughness, σ (eqs S14 and S15 and Figure S8). Theoretical atomic roughness was calculated to range within 0.8–1.4 Å for our OD-Cu models (Figure S9); thus, it was significantly higher than experimental values for crystalline Cu, 0.32 Å.[66] For red-Cu$_2$O systems, surface roughness did not change significantly after equilibration, while oxi-Cu surfaces kept reconstructing until σ = 1.5, 1.1, and 1.0 Å for 4R, 4T, and 6L, respectively, until 8 ps AIMD time, because of the geometric stress between metallic and oxidic layers. The ratio of surface sites of the reconstructed surfaces versus surface sites of crystalline Cu$_2$O(111) increases by 120% (140%) for red-Cu$_2$O (oxi-Cu) with regard to pristine oxidic copper (Figure S10 and eq S16), in line with the increased electrochemically active surface area on OD-Cu.[7] 6L-oxi-Cu presents the largest increment of surface sites among all the configurations, albeit showing the lowest atomic surface roughness. Therefore, we identify grain boundaries as minor perturbations of the surface which determine mild surface roughness but large active area, as suggested experimentally.[34] In contrast, reconstruction strongly modified rhomboidal (4R) and triangular configurations (4T), increasing surface roughness (Figure 1c,d and Videos S1–S7[55]).

To determine the local coordination of Cu atoms, we calculated Cu–Cu and Cu–O RDFs, g_{Cu-O} and g_{Cu-Cu} (eqs S17 and S18). For all the systems, g_{Cu-O} shows a well-defined minimum at a Cu–O distance of 2.50 Å, which is between the first and second peaks of bulk Cu$_2$O: 1.87 and 3.57 Å (Figure S11). Thus, we set d_{Cu-O} = 2.50 Å as threshold for O coordination to Cu. Consequently, we found that Cu exists in three well-defined states according to its coordination to
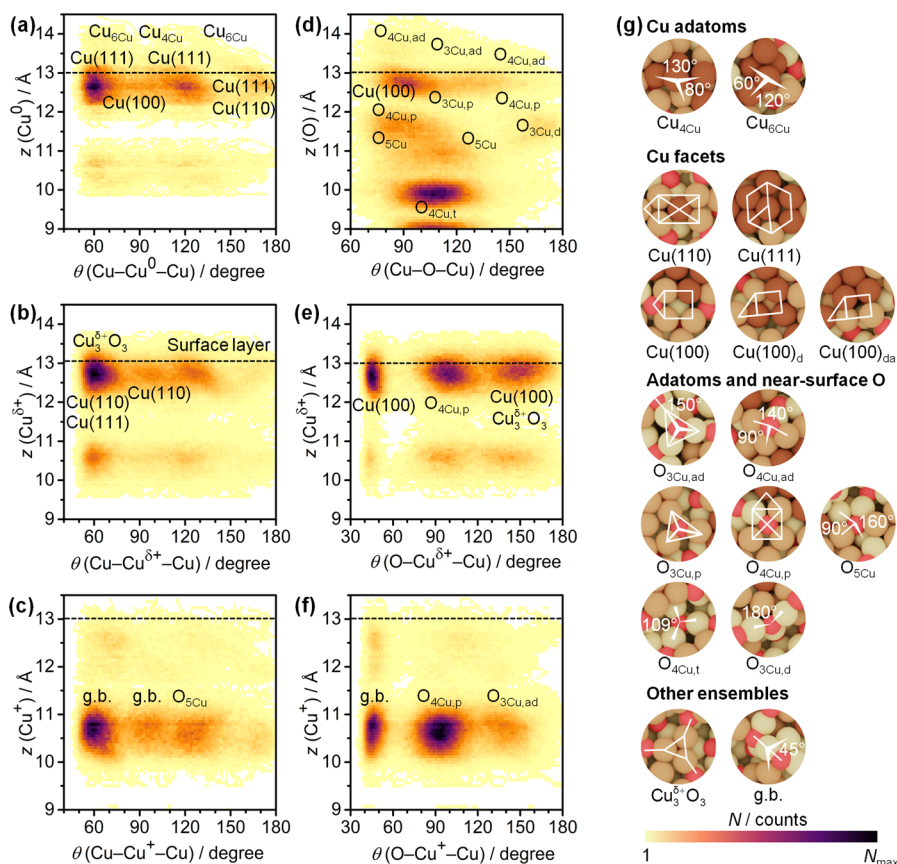
Figure 3. Recurrent ensembles in OD-Cu models. (a–f) Histograms for angles $\theta(A-B-C)$ measured around the first coordination shell of central atom B at different heights $z(B)$ for the 4R-red-Cu_2O system. The ensembles responsible for each feature are labeled and shown in panel g; tetra- and hexa-coordinated Cu adatoms: Cu_{3Cu} and Cu_{4Cu}; reminiscent of crystalline Cu: Cu(100)-like facets, including distorted forms mainly metallic or asymmetric in charge (subscripts "d" and "da"), Cu(110) and Cu(111) facets; $Cu_3^{\delta+}O_3$; Cu/Cu_2O grain boundaries, g.b. (Figure S2); tri- and tetra-coordinated O adatoms: $O_{3Cu,ad}$ and $O_{4Cu,ad}$; tri- and tetra-coordinated planar O: $O_{3Cu,p}$ and $O_{4Cu,p}$; penta-coordinated near-surface O: O_{5Cu}; tetrahedral O: $O_{4Cu,t}$; distorted near-surface O: $O_{3Cu,d}$. Comparison with other models and values of N_{max} are reported in Figures S21 and S22.

nearby oxygen atoms: metallic, suboxidic, and oxidic Cu (Figure 2). Suboxidic $Cu_2O_{0.5}$-like species have been also detected experimentally,[30,47,64] and EXAFS characterization confirmed an average Cu–O coordination number of 1.1 for suboxidic Cu.[64] Despite presenting different stoichiometry (31, 13, and 11 atom % O) and initial configurations (Table S3), all the models gave comparable RDFs upon AIMD, thus reinforcing the general nature of our results (Figures 2a–f and S12).

The first Cu–Cu coordination shell is a combination of crystalline Cu and Cu_2O, somewhat smeared in the intermediate values (Figure 2a–f). To calculate the coordination number of each Cu to neighboring Cu atoms, N_{Cu-Cu}, we counted 1 bond when the Cu–Cu distance was the one of metallic Cu, no bonds for the one of Cu_2O, and applied a Gaussian smearing for the values in between (eqs S19–20 and Figure S13). The distribution of $\bar{N}_{Cu-Cu}$ values averaged over time does not show significant changes for red-Cu_2O models (Figure S14). In contrast, oxi-Cu systems again reveal a continuous reconstruction process until 6 ps, where metallic-like configurations reform from pristine low coordinated Cu. As a general trend, Cu is undercoordinated when compared to typical values for crystalline facets (Table S8). When coordinated to 1 oxygen, copper atoms lose 1 Cu bond; thus, $\bar{N}_{Cu-Cu} \approx 4$ (5) for the two families of models. Finally,

double O coordination saturates Cu sites; thus, $\bar{N}_{Cu-Cu}$ further decreases by 2 metallic bonds, ∼2 (3) for red-Cu_2O (oxi-Cu). In agreement with our theoretical predictions of $\bar{N}_{Cu-Cu}$ = 4.9, 3.6, and 2.0 for metallic, suboxidic, and oxidic copper, respectively (Figure 2h–j), $\bar{N}_{Cu-Cu}$ of 6.6, 3.08, 2.21, and 1.84 have been experimentally reported for OD-Cu systems.[64,67]

Moving ahead to address key contributors to OD-Cu performance, we then targeted Cu electronic structure.[6,15,20,22,38] We sampled the Bader charges for the whole simulation period at a time step of 48 fs. Because the seven models feature analogous structural properties (Figures 2a–f and S12) we focused the analysis on the 4R-red-Cu_2O system, whereas the characterization of other models is reported in Figure S15. As shown in Figure 2g, the three Cu species described in the previous section account for well-defined oxidation states. Metallic and oxidic Cu charges are centered at 0.0 and 0.5 |e⁻|, respectively, akin to bulk Cu and Cu_2O. We labeled these species as metallic, Cu^0, and oxidic copper, Cu^+. Cu atoms coordinated with one oxygen exhibit intermediate positive polarization with a well-defined boundary between 0.1 ≤ q_{Cu} ≤ 0.4 |e⁻|. Thus, we assign this species to the previously proposed polarized Cu, also called "suboxidic", $Cu^{\delta+}$.[30,47,64]

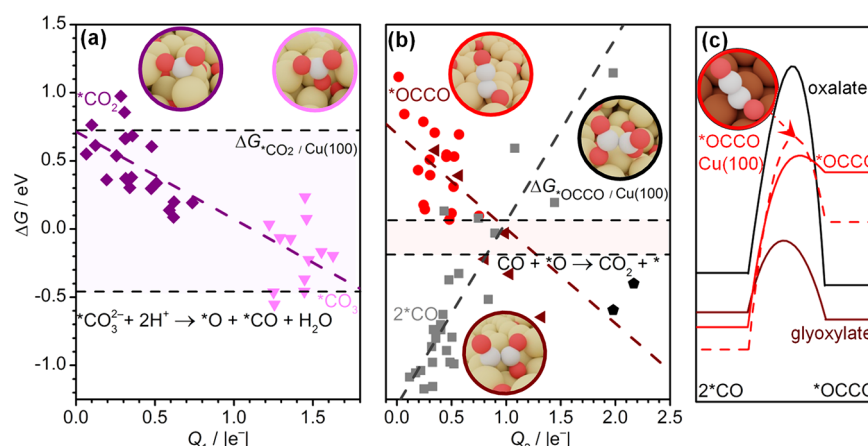The relative abundance of these three species depends on the initial configuration and stoichiometry (Figure S16 and

Figure 4. CO_2R activity and C_{2+} selectivity of OD-Cu versus ensemble polarization. (a) OD-Cu can adsorb CO_2 either on a Cu site (purple) or on a near-surface oxygen (magenta) forming a carbonate. CO_2 adsorption energy scales linearly with the polarization of the active sites, Q_1: $\Delta G_{*CO_2} = +0.7(\pm 0.1) - 0.6(\pm 0.1)Q_1$. $Cu^0-Cu^{\delta+}$ and $Cu^{\delta+}-Cu^{\delta+}$ are responsible for enhancing OD-Cu CO_2R (purple area), while activity of O_{ns} sites is limited by carbonate formation. (b) Polarization of active ensembles, Q_2, drives selectivity to C_2 products: $\Delta G_{*OCCO} = +0.7(\pm 0.1) - 0.7(\pm 0.1)Q_2$. A paired active site, $Cu^{\delta+}$-O_{ns}, stabilizes the CO−CO dimer as a glyoxylate-like intermediate (dark red), enhancing C_2 production. In contrast, for metallic Cu sites (red) CO dimerization is not favored, leading to a higher *CO coverage (gray), $\Delta G_{2*CO} = -1.3(\pm 0.1) + 1.3(\pm 0.1)Q_2$. For very strong polarization, stable oxalates are generated on the surface (black). Q_1 and Q_2 are defined as the sum of absolute Bader charges of the atoms in the ensemble calculated with implicit solvation (eqs S21 and S22, Figure S27). (c) *OCCO intermediate on both OD-Cu and Cu(100) and oxalate formation on OD-Cu presents a high kinetic barrier of more than 1 eV. The pathway toward the glyoxylate-like intermediate has instead a mild barrier of 0.53 eV. Potential and dipole corrections, here not included, stabilize all intermediates similarly (Table S16). Further details on the linear regressions are shown in Table S17.

Table S9). Red-Cu_2O accounts high abundance of $Cu^{\delta+}/Cu^+$ sites, while the stronger reconstruction occurring on oxi-Cu systems determines an increase of Cu^+ species. Metallic copper is instead favored by low O atomic percentage, as expected for the SY-red-Cu_2O system. The presence of residual Cu^+ species upon reconstruction agrees with recent experimental reports for Cu_2O nanocubes (20% at −0.95 V vs RHE) and Cu(100) under CO_2 pulsed electroreduction (7−11% at −1 V vs RHE).[6,42] N_{Cu-Cu} cumulative maps prove the existence of atomic ensembles for all the three classes: metallic Cu^0 (Figure 2j), polarized $Cu^{\delta+}$ (Figure 2i), and oxidic Cu^+ (Figure 2h). The analysis of the remaining models support this finding (Figure S17).

In addition to averaged properties, a unequivocal identification of recurrent ensembles requires local characterization. Atomic ensembles are defined by their interatomic distances and angles. Therefore, we mapped the occurrence of interatomic angles versus the z-coordinate of the central atom to identify its coordination environment. As a result we detected 14 recurrent ensembles which were stable at different AIMD temperatures, Figure S18−S19, and with Hubbard correction, Figure S20. As a 2-dimensional histogram, darker areas represent higher density of atoms with a given angle with neighboring sites at a given z-coordinate, within the two outermost layers, Figure 3a-f and Figures S21−S22. For metallic copper, Cu^0, we identified a few 4- and 6-coordinated Cu adatoms, $Cu_{4Cu}-Cu_{6Cu}$. In addition, surface reconstructs into reminiscent of crystalline domains, such as Cu(100), Cu(110), and Cu(111), either fully metallic or including few polarized $Cu^{\delta+}$. Few surface $Cu^{\delta+}$ species aggregate in triangular $Cu_3^{\delta+}O_3$ ensembles. This ensemble has been characterized experimentally very recently in ref 30, and reconstruction of Cu-based catalysts toward open facets was detected through *operando* electrochemical STM.[9,44] Oxidic Cu^+ is not abundant at the outermost layers, and the interface between Cu^+ and $Cu^0-Cu^{\delta+}$ species mimics the grain

boundary motif reported in Figure S2. Regarding the oxygen atoms, their preferred configuration depends on their position. Inner atoms adopt mainly bulk-like tetrahedral shapes, $O_{4Cu,t}$, as well as few distorted configurations with 3-fold or 5-fold coordination, $O_{3Cu,d}$, O_{5Cu}. Besides, there is a strong, narrow signal at 45° which is characteristic of a "grain boundary" ensemble (g.b. in Figure 3g). Near-surface oxygens (O_{ns}) prefer to adopt planar configurations, namely $O_{3Cu,p}$ and $O_{4Cu,p}$. Finally, oxygen adatoms may coordinate with three or four Cu atoms, $O_{3Cu,ad}$ and $O_{4Cu,ad}$. These adatoms give a mild and diffuse signal, meaning that they are less abundant than near-surface configurations and do not have any strong preference to adopt a particular shape. In recent experiments, near-surface oxygen has been found stable in $Cu_2O_{0.5}$ stoichiometry at potentials as reductive as −1.0 V vs RHE,[64] but there is scarce experimental information about the remaining oxygen ensembles.

Previous computational studies assessed the catalytic properties of very ordered systems,[3,51] including O as an impurity in crystalline Cu for modeling OD-Cu catalysts.[39,46,48] Our analysis proves that the landscape of OD-Cu catalysts might be much more complex because of the appearance of several new ensembles. Because metastable states, even if less abundant, can be the active sites which drive the activity and selectivity of metals and oxides,[54] here we investigated the adsorption properties of the identified ensembles to obtain new potential descriptors for CO_2 reduction on OD-Cu. We evaluated *CO_2, *OCCO, and 2*CO adsorption energies, as these molecules are generally reported as the key intermediates for CO_2R activity and C_{2+} selectivity.[2] Because local configurations do not change significantly among red-Cu_2O and oxi-Cu models (Figures S21 and S22), we sampled only the first ones.

Our simulations show that CO_2 adsorbs via Cu−C and Cu−O bonds, $\eta^2_{C,O}$, on Cu sites (Figure 4a, purple), or via a O_{ns}−C bond on near-surface O (Figure 4a, magenta). CO_2 adsorption

energy scales linearly with the polarization of the ensembles, approximated by Q_1, the sum of their Bader charges in absolute value (eqs S21 and S22). $X^{\delta-}-Cu^{\delta+}$ (X = O, Cu^0) asymmetric pairs are strong binding sites for CO_2 because of high polarization. $Cu^0-Cu^{\delta+}$ and $Cu^{\delta+}-Cu^{\delta+}$ pairs in ensembles Cu_{4Cu}, Cu_{6Cu}, and $Cu_3^{\delta+}O_3$ (Figure 3g) can tether CO_2 more favorably than crystalline copper by 0.5 eV (0.2 eV vs 0.7 eV, Table S10). Cu^+ sites, saturated by the 2 neighboring O atoms, do not play a relevant catalytic role (Figure S23). In the literature, the specific role of the $Cu^0_{adatom}-Cu^{\delta+}(Cu^+)$ pair on CO_2 activation has been suggested.[39,68] Here, we provide a generalized model, proposing negative (positive) polarization on C (O) binding sites as a general descriptor for CO_2 activity. As experimental evidence, CO_2 adsorption has been detected via SEIRAS spectroscopy at low overpotential for suboxidic and oxidic Cu.[15] High local polarization accounts for the remarkable performance of OD-Cu, along with higher surface roughness and number of active sites (Figures S9 and S10). The high electronic density localized on near-surface $O_{3Cu,p}$ and $O_{4Cu,p}$ oxygens (Figure 3g) saturates the $O_{ns}-C$ bond; thus, it leads to saturation of CO_2 binding energy to high exothermic values (Figure S24). As a consequence, the surface is passivated from carbonate coverage, and it is not active anymore for CO_2 reduction.[38] Carbonate coverage has been reported on OD-Cu under CO_2 reduction conditions via in situ and real-time surface-enhanced infrared absorption spectroscopy (SEIRAS) (Table S11).

Because CO_2 reduction activity is promoted by local polarization, we now focus on the CO—CO dimer, whose stability on the surface has been proposed to determine CO_2 selectivity and therefore C_{2+} product distribution.[2,32] In Figure 4b we present the stability of the dimer for the identified local ensembles. Again, the adsorption energy for the dimer depends linearly on the sum of the Bader charges of the ensembles, Q_2, proxy of their polarization (eqs S21 and S22). We can identify 3 types of adsorbed species: CO—CO dimer, *OCCO; glyoxylate-like intermediates, *OCCOO; and oxalate, *OOCCOO. Metal-only domains generate CO—CO dimers (Figure 4b, red inset), which are easily dissociated, therefore leading to similar product distribution as copper foil and nanoparticles (H_2, CH_4).[12,14] Polarized $Cu^0-Cu^{\delta+}$ (100)—(110) facets (Figure 3g) exhibit similar reactivity as crystalline Cu(100) (Table S10), thus confirming the experimental hypotheses on structural and chemical affinity between crystalline open facets and OD-Cu.[27,35] For very high surface polarization, strongly bound oxalates are generated on the surface via two near-surface oxygens (Figure 4b, black inset). If formed, oxalates could cause surface passivation and Cu dissolution; however, this process is hindered by the high kinetic barrier associated, 1.51 eV (Figure 4c, black inset). Furthermore, if oxygen sites tether CO too strongly, they may desorb as CO_2 (lower dashed line in Figure 4b and Table S12). Mild surface polarization makes CO—CO formation thermoneutral; therefore, it enables the dimerization reaction.[69,70] Glyoxylate-like species OC*CO-(O_{ns}) triggers OD-Cu selectivity to C_{2+} because of the low kinetic barrier associated to its formation, 0.53 eV (Figure 4b-c, dark red inset). The carbon atoms of this intermediate are separately adsorbed on a bridge position between low coordinated Cu and atop a near-surface oxygen. The local Cu coordination resembles either Cu(111) facets or the $Cu_3^{\delta+}O_3$ ensemble previously reported (ref 71) (Figure S25). Glyoxylate is a well-known intermediate for prebiotic CO_2 reduction,[72] although to the best of our knowledge its

dehydrogenated form, OC*CO(O_{ns}), has not yet been reported in electrochemical CO_2 literature.[31,73] We highlight that glyoxylate and oxalate production may occur as well via direct CO_2 reduction (Table S13) and that glyoxylate vibrational frequencies (1630, 1479, and 1145 cm^{-1}; Table S14) are compatible with SEIRAS and IR spectroscopy signals for CO_2 reduction on OD-Cu (Tables S11 and S15). We therefore propose the paired $Cu^{\delta+}-O_{ns}$ active site that stabilizes the glyoxylate-like intermediate to open the pathway for ethanol production on OD-Cu at −0.25 V vs RHE,[17] as a weak metal—oxygen bond has been deemed responsible for alcohol production on Cu.[74]

The product distribution of OD-Cu depends on time and can be attributed to the relative abundance of the different ensembles under CO_2R conditions.[6] Low-coordinated Cu^0 sites (Cu_{6Cu}, Cu_{4Cu}, and $Cu_3^{\delta+}O_3$; Figure 3g) present stronger CO binding energy than crystalline Cu (Figure S23). Therefore, we identify them with the strong binding sites reported on OD-Cu by Verdaguer-Casadevall et al.[75] $Cu^{\delta+}$ coordination tunes significantly its adsorption properties: ΔE_{*CO} ranges from −0.5 to +0.5 eV (Figure S23). Local coordination and oxidation state influences Cu affinity to oxygen: both Cu^0 and $Cu^{\delta+}$ are less oxophilic than Cu(100), and an increasing oxidation state leads to lower O affinity (Figure S23). The rationale of the wide OD-Cu product distribution may then be elucidated by Cu coordination and its affinity to O; thus, those descriptors could be applied in the future to explain the occurrence of specific active sites toward ethylene, ethanol, and n-propanol.[10]

We have compiled and identified three key contributions toward OD-Cu activity and C_{2+} selectivity: polarized active sites, open facets, and glyoxylate route. Local charge polarization strengthens CO_2 binding, thus promoting a higher CO_2R activity. This insight provides a solid understanding of the role of $Cu^{\delta+}$ as a privileged site for OD-Cu catalysts.[6,15,20,22,38] Reconstructed open facets resemble crystalline Cu(100), thus motivating ethylene production at high onset potential. The $Cu^{\delta+}-O_{ns}$ pair adsorbs the CO dimer exothermically as a glyoxylate-like intermediate, which accounts for the low onset potential toward C_{2+} products reported experimentally.[17]

In the present work we characterized oxide-derived copper catalysts at different stoichiometries and oxidation stages. After ab initio molecular dynamics simulations, the final structures present high surface area and atomic-scale roughness. Independently from the initial model assumed, Cu exists as three species: Cu^0, $Cu^{\delta+}$, and Cu^+, which combine into 14 well-defined ensembles. Among those ensembles, $Cu^{\delta+}$, $Cu^0-Cu^{\delta+}$, and $Cu-O_{ns}$ are the active and selective sites for CO_2 reduction. $Cu^{\delta+}$ and $Cu^0-Cu^{\delta+}$ tether CO_2 actively because of their high polarization, thus promoting CO_2 activation. The $Cu-O_{ns}$ pair stabilizes C—C coupling via a glyoxylate-like intermediate, which opens the reaction pathway toward C_{2+} products from −0.5 V vs RHE because of the low kinetic barrier associated with its formation, 0.53 eV. O_{ns} is here reported stable until −0.84 V vs RHE in good agreement with recent experimental reports.[64] Although our methodology does not include solvent, electrolyte, adsorbates, and electric field during ab initio molecular dynamics, the results are qualitatively robust and constitute a step forward in the understanding of the role of new ensembles on oxide-derived copper reactivity. Our study conciliates all the previous experimental observations concerning the nature of OD-Cu

active sites during CO_2 reduction time-scales and the consequent changes in product distribution. As active and selective sites have been characterized, the core of future investigations must be the development of synthetic protocols to stabilize these privileged ensembles.

■ ASSOCIATED CONTENT

ⓢ Supporting Information

The Supporting Information is available free of charge at https://pubs.acs.org/doi/10.1021/acsenergylett.0c01777.

Computational methods, supporting discussion, eqs S1–S24, Figures S1–S27, and Tables S1–S20 (PDF)

■ AUTHOR INFORMATION

Corresponding Author

Núria López − *Institute of Chemical Research of Catalonia (ICIQ), The Barcelona Institute of Science and Technology (BIST), 43007 Tarragona, Spain;* Ⓞorcid.org/0000-0001-9150-5941; Email: nlopez@iciq.es

Authors

Federico Dattila − *Institute of Chemical Research of Catalonia (ICIQ), The Barcelona Institute of Science and Technology (BIST), 43007 Tarragona, Spain;* Ⓞorcid.org/0000-0001-8195-3951

Rodrigo García-Muelas − *Institute of Chemical Research of Catalonia (ICIQ), The Barcelona Institute of Science and Technology (BIST), 43007 Tarragona, Spain;* Ⓞorcid.org/0000-0002-2219-5027

Complete contact information is available at:
https://pubs.acs.org/10.1021/acsenergylett.0c01777

Notes

The authors declare no competing financial interest.
The data sets generated during the current study and the full *ab initio* molecular dynamics trajectories for red-Cu_2O and oxi-Cu systems, Videos S1–S7,[55] are available in the ioChem-BD database[76] at DOI 10.19061/iochem-bd-1-165.

■ ACKNOWLEDGMENTS

■ REFERENCES

(1) Nitopi, S.; et al. Progress and perspectives of electrochemical CO_2 reduction on copper in aqueous electrolyte. *Chem. Rev.* **2019**, *119*, 7610−7672.

(2) Birdja, Y. Y.; Pérez-Gallent, E.; Figueiredo, M. C.; Göttle, A. J.; Calle-Vallejo, F.; Koper, M. T. M. Advances and challenges in understanding the electrocatalytic conversion of carbon dioxide to fuels. *Nat. Energy* **2019**, *4*, 732−745.

(3) Peterson, A. A.; Abild-Pedersen, F.; Studt, F.; Rossmeisl, J.; Nørskov, J. K. How copper catalyzes the electroreduction of carbon dioxide into hydrocarbon fuels. *Energy Environ. Sci.* **2010**, *3*, 1311−1315.

(4) Hori, Y.; Murata, A.; Takahashi, R. Formation of hydrocarbons in the electrochemical reduction of carbon dioxide at a copper electrode in aqueous solution. *J. Chem. Soc., Faraday Trans. 1* **1989**, *85*, 2309−2326.

(5) De Luna, P.; Hahn, C.; Higgins, D.; Jaffer, S. A.; Jaramillo, T. F.; Sargent, E. H. What would it take for renewably powered electrosynthesis to displace petrochemical processes? *Science* **2019**, *364*, 350.

(6) Arán-Ais, R. M.; Scholten, F.; Kunze, S.; Rizo, R.; Roldan Cuenya, B. The role of in situ generated morphological motifs and Cu(I) species in C_{2+} product selectivity during CO_2 pulsed electroreduction. *Nat. Energy* **2020**, *5*, 317−325.

(7) Gao, D.; Arán-Ais, R. M.; Jeon, H. S.; Roldán-Cuenya, B. Rational catalyst and electrolyte design for CO_2 electroreduction towards multicarbon products. *Nat. Catal.* **2019**, *2*, 198−210.

(8) Huang, J.; Hörmann, N.; Oveisi, E.; Loiudice, A.; De Gregorio, G. L.; Andreussi, O.; Marzari, N.; Buonsanti, R. Potential-induced nanoclustering of metallic catalysts during electrochemical CO_2 reduction. *Nat. Commun.* **2018**, *9*, 3117.

(9) Kim, Y. G.; Baricuatro, J. H.; Javier, A.; Gregoire, J. M.; Soriaga, M. P. The evolution of the polycrystalline copper surface, first to Cu(111) and then to Cu(100), at a fixed CO_2RR potential: A study by operando EC-STM. *Langmuir* **2014**, *30*, 15053−15056.

(10) Lum, Y.; Ager, J. W. Evidence for product-specific active sites on oxide-derived Cu catalysts for electrochemical CO_2 reduction. *Nat. Catal.* **2019**, *2*, 86−93.

(11) Auer, A.; Andersen, M.; Wernig, E.-M.; Hörmann, N. G.; Buller, N.; Reuter, K.; Kunze-Liebhäuser, J. Self-activation of copper electrodes during CO electro-oxidation in alkaline electrolyte. *Nat. Catal.* **2020**, DOI: 10.1038/s41929-020-00505-w.

(12) Hori, Y.; Takahashi, I.; Koga, O.; Hoshi, N. Electrochemical reduction of carbon dioxide at various series of copper single crystal electrodes. *J. Mol. Catal. A: Chem.* **2003**, *199*, 39−47.

(13) Kuhl, K. P.; Cave, E. R.; Abram, D. N.; Jaramillo, T. F. New insights into the electrochemical reduction of carbon dioxide on metallic copper surfaces. *Energy Environ. Sci.* **2012**, *5*, 7050−7059.

(14) Reske, R.; Mistry, H.; Behafarid, F.; Roldan Cuenya, B.; Strasser, P. Particle size effects in the catalytic electroreduction of CO_2 on Cu nanoparticles. *J. Am. Chem. Soc.* **2014**, *136*, 6978−6986.

(15) Chou, T.-C.; et al. Controlling the oxidation state of Cu electrode and reaction intermediates for electrochemical CO_2 reduction to ethylene. *J. Am. Chem. Soc.* **2020**, *142*, 2857−2867.

(16) Li, C. W.; Kanan, M. W. CO_2 reduction at low overpotential on Cu electrodes resulting from the reduction of thick Cu_2O films. *J. Am. Chem. Soc.* **2012**, *134*, 7231−7234.

(17) Li, C. W.; Ciston, J.; Kanan, M. W. Electroreduction of carbon monoxide to liquid fuel on oxide-derived nanocrystalline copper. *Nature* **2014**, *508*, 504−507.

(18) Ren, D.; Deng, Y.; Handoko, A. D.; Chen, C. S.; Malkhandi, S.; Yeo, B. S. Selective electrochemical reduction of carbon dioxide to ethylene and ethanol on copper(I) oxide catalysts. *ACS Catal.* **2015**, *5*, 2814−2821.

(19) Kim, D.; Lee, S.; Ocon, J. D.; Jeong, B.; Lee, J. K.; Lee, J. Insights into an autonomously formed oxygen-evacuated Cu_2O electrode for the selective production of C_2H_4 from CO_2. *Phys. Chem. Chem. Phys.* **2015**, *17*, 824−830.

(20) Mistry, H.; et al. Highly selective plasma-activated copper catalysts for carbon dioxide reduction to ethylene. *Nat. Commun.* **2016**, *7*, 12123.

(21) Handoko, A. D.; Ong, C. W.; Huang, Y.; Lee, Z. G.; Lin, L.; Panetti, G. B.; Yeo, B. S. Mechanistic insights into the selective electroreduction of carbon dioxide to ethylene on Cu_2O-derived copper catalysts. *J. Phys. Chem. C* **2016**, *120*, 20058−20067.

(22) De Luna, P.; Quintero-Bermudez, R.; Dinh, C.-T.; Ross, M. B.; Bushuyev, O. S.; Todorović, P.; Regier, T.; Kelley, S. O.; Yang, P.; Sargent, E. H. Catalyst electro-redeposition controls morphology and oxidation state for selective carbon dioxide reduction. *Nat. Catal.* **2018**, *1*, 103−110.

(23) Lee, S. Y.; Jung, H.; Kim, N.-K.; Oh, H.-S.; Min, B. K.; Hwang, Y. J. Mixed copper states in anodized Cu electrocatalyst for stable and

selective ethylene production from CO_2 reduction. *J. Am. Chem. Soc.* **2018**, *140*, 8681−8689.

(24) Li, J.; et al. Copper adparticle enabled selective electrosynthesis of *n*-propanol. *Nat. Commun.* **2018**, *9*, 4614.

(25) Ting, L. R. L.; Garcia-Muelas, R.; Martin, A. J; Veenstra, F. L. P.; Chen, S. T.-J.; Peng, Y.; Per, E. Y. X.; Pablo Garcia, S.; Lopez, N.; Perez-Ramirez, J.; Yeo, B. S. Electrochemical reduction of carbon dioxide to 1-butanol on oxide-derived copper. *Angew. Chem., Int. Ed.* **2020**, *25*, 2−10.

(26) Dutta, A.; Rahaman, M.; Luedi, N. C.; Mohos, M.; Broekmann, P. Morphology matters: tuning the product distribution of CO_2 electroreduction on oxide-derived Cu foam catalysts. *ACS Catal.* **2016**, *6*, 3804−3814.

(27) Loiudice, A.; Lobaccaro, P.; Kamali, E. A.; Thao, T.; Huang, B. H.; Ager, J. W.; Buonsanti, R. Tailoring copper nanocrystals towards C_2 products in electrochemical CO_2 reduction. *Angew. Chem., Int. Ed.* **2016**, *55*, 5789−5792.

(28) Lum, Y.; Ager, J. W. Stability of residual oxides in oxide-derived copper catalysts for electrochemical CO_2 reduction investigated with ^{18}O labeling. *Angew. Chem., Int. Ed.* **2018**, *57*, 551−554.

(29) Zhu, Q.; Sun, X.; Yang, D.; Ma, J.; Kang, X.; Zheng, L.; Zhang, J.; Wu, Z.; Han, B. Carbon dioxide electroreduction to C_2 products over copper-cuprous oxide derived from electrosynthesized copper complex. *Nat. Commun.* **2019**, *10*, 3851.

(30) Lin, S.-C.; Chang, C.-C.; Chiu, S.-Y.; Pai, H.-T.; Liao, T.-Y.; Hsu, C.-S.; Chiang, W.-H.; Tsai, M.-K.; Chen, H. M. Operando time-resolved X-ray absorption spectroscopy reveals the chemical nature enabling highly selective CO_2 reduction. *Nat. Commun.* **2020**, *11*, 3525.

(31) Kortlever, R.; Shen, J.; Schouten, K. J. P.; Calle-Vallejo, F.; Koper, M. T. M. Catalysts and reaction pathways for the electrochemical reduction of carbon dioxide. *J. Phys. Chem. Lett.* **2015**, *6*, 4073−4082.

(32) Pérez-Gallent, E.; Figueiredo, M. C.; Calle-Vallejo, F.; Koper, M. T. M. Spectroscopic observation of a hydrogenated CO dimer intermediate during CO reduction on Cu(100) electrodes. *Angew. Chem., Int. Ed.* **2017**, *56*, 3621−3624.

(33) Cheng, T.; Xiao, H.; Goddard, W. A. Nature of the active sites for CO reduction on copper nanoparticles; Suggestions for optimizing performance. *J. Am. Chem. Soc.* **2017**, *139*, 11642−11645.

(34) Feng, X.; Jiang, K.; Fan, S.; Kanan, M. W. A direct grain-boundary-activity correlation for CO electroreduction on Cu nanoparticles. *ACS Cent. Sci.* **2016**, *2*, 169−174.

(35) Wang, Y.; et al. Catalyst synthesis under CO_2 electroreduction favours faceting and promotes renewable fuels electrosynthesis. *Nat. Catal.* **2020**, *3*, 98−106.

(36) Ringe, S.; Morales-Guio, C. G.; Chen, L. D.; Fields, M.; Jaramillo, T. F.; Hahn, C.; Chan, K. Double layer charging driven carbon dioxide adsorption limits the rate of electrochemical carbon dioxide reduction on Gold. *Nat. Commun.* **2020**, *11*, 33.

(37) Veenstra, F. L.; Ackerl, N.; Martín, A. J.; Pérez-Ramírez, J. Laser-microstructured copper reveals selectivity patterns in the electrocatalytic reduction of CO_2. *Chem.* **2020**, *6*, 1707−1722.

(38) Velasco-Vélez, J.-J.; et al. The role of the copper oxidation state in the electrocatalytic reduction of CO_2 into valuable hydrocarbons. *ACS Sustainable Chem. Eng.* **2019**, *7*, 1485−1492.

(39) Favaro, M.; Xiao, H.; Cheng, T.; Goddard, W. A.; Yano, J.; Crumlin, E. J. Subsurface oxide plays a critical role in CO_2 activation by Cu(111) surfaces to form chemisorbed CO_2, the first step in reduction of CO_2. *Proc. Natl. Acad. Sci. U. S. A.* **2017**, *114*, 6706−6711.

(40) Velasco-Velez, J.-J.; et al. Revealing the active phase of copper during the electroreduction of CO_2 in aqueous electrolyte by correlating *In Situ* X-ray spectroscopy and *In Situ* electron microscopy. *ACS Energy Lett.* **2020**, *5*, 2106−2111.

(41) Zhao, Y.; Chang, X.; Malkani, A. S.; Yang, X.; Thompson, L.; Jiao, F.; Xu, B. Speciation of Cu surfaces during the electrochemical CO reduction reaction. *J. Am. Chem. Soc.* **2020**, *142*, 9735−9743.

(42) Möller, T.; et al. Electrocatalytic CO_2 reduction on CuO_x nanocubes tracking the evolution of chemical state, geometric structure, and catalytic selectivity using Operando Spectroscopy. *Angew. Chem., Int. Ed.* **2020**, DOI: 10.1002/anie.202007136.

(43) He, M.; Li, C.; Zhang, H.; Chang, X.; Chen, J. G.; Goddard, W. A., III; Cheng, M.-j.; Xu, B.; Lu, Q. Oxygen induced promotion of electrochemical reduction of CO_2 via co-electrolysis. *Nat. Commun.* **2020**, *11*, 3844.

(44) Kim, Y. G.; Soriaga, M. P. Cathodic regeneration of a clean and ordered Cu(100)-(1 × 1) surface from an air-oxidized and disordered electrode: An operando STM study. *J. Electroanal. Chem.* **2014**, *734*, 7−9.

(45) Scott, S. B.; et al. Absence of oxidized phases in Cu under CO reduction conditions. *ACS Energy Lett.* **2019**, *4*, 803−804.

(46) Eilert, A.; et al. Subsurface oxygen in oxide-derived copper electrocatalysts for carbon dioxide reduction. *J. Phys. Chem. Lett.* **2017**, *8*, 285−290.

(47) Schedel-Niedrig, T.; Neisius, T.; Böttger, I.; Kitzelmann, E.; Weinberg, G.; Demuth, D.; Schlögl, R. Copper (sub)oxide formation: a surface sensitive characterization of model catalysts. *Phys. Chem. Chem. Phys.* **2000**, *2*, 2407−2417.

(48) Liu, C.; Lourenço, M. P.; Hedström, S.; Cavalca, F.; Diaz-Morales, O.; Duarte, H. A.; Nilsson, A.; Pettersson, L. G. Stability and effects of subsurface oxygen in oxide-derived Cu catalyst for CO_2 reduction. *J. Phys. Chem. C* **2017**, *121*, 25010−25017.

(49) Garza, A. J.; Bell, A. T.; Head-Gordon, M. Is subsurface oxygen necessary for the electrochemical reduction of CO_2 on copper? *J. Phys. Chem. C* **2018**, *9*, 601−606.

(50) Fields, M.; Hong, X.; Nørskov, J. K.; Chan, K. Role of subsurface oxygen on Cu surfaces for CO_2 electrochemical reduction. *J. Phys. Chem. C* **2018**, *122*, 16209−16215.

(51) Bagger, A.; Ju, W.; Varela, A. S.; Strasser, P.; Rossmeisl, J. Electrochemical CO_2 reduction: Classifying Cu facets. *ACS Catal.* **2019**, *9*, 7894−7899.

(52) Calle-Vallejo, F.; Tymoczko, J.; Colic, V.; Vu, Q. H.; Pohl, M. D.; Morgenstern, K.; Loffreda, D.; Sautet, P.; Schuhmann, W.; Bandarenka, A. S. Finding optimal surface sites on heterogeneous catalysts by counting nearest neighbors. *Science* **2015**, *350*, 185−189.

(53) Fung, V.; Tao, F. F.; Jiang, D. E. General structure-reactivity relationship for oxygen on transition-metal oxides. *J. Phys. Chem. Lett.* **2017**, *8*, 2206−2211.

(54) Zhang, Z.; Zandkarimi, B.; Alexandrova, A. N. Ensembles of metastable states govern heterogeneous catalysis on dynamic interfaces. *Acc. Chem. Res.* **2020**, *53*, 447−458.

(55) Dattila, F. Supporting Videos 1−7; https://iochem-bd.iciq.es/browse/handle/100/26145, 2020 (accessed 2020-07-24).

(56) Yang, F.; Choi, Y.; Liu, P.; Hrbek, J.; Rodriguez, J. A. Autocatalytic reduction of a Cu_2O/Cu(111) surface by CO: STM, XPS, and DFT studies. *J. Phys. Chem. C* **2010**, *114*, 17042−17050.

(57) Perdew, J. P.; Burke, K.; Ernzerhof, M. Generalized gradient approximation made simple. *Phys. Rev. Lett.* **1996**, *77*, 3865−3868.

(58) Fishman, M.; Zhuang, H. L.; Mathew, K.; Dirschka, W.; Hennig, R. G. Accuracy of exchange-correlation functionals and effect of solvation on the surface energy of copper. *Phys. Rev. B: Condens. Matter Mater. Phys.* **2013**, *87*, 245402.

(59) Mathew, K.; Sundararaman, R.; Letchworth-Weaver, K.; Arias, T. A.; Hennig, R. G. Implicit solvation model for density-functional study of nanocrystal surfaces and reaction pathways. *J. Chem. Phys.* **2014**, *140*, 084106.

(60) Singh, A. K.; Zhou, L.; Shinde, A.; Suram, S. K.; Montoya, J. H.; Winston, D.; Gregoire, J. M.; Persson, K. A. Electrochemical stability of metastable materials. *Chem. Mater.* **2017**, *29*, 10159−10167.

(61) Guan, R.; Hashimoto, H.; Kuo, K. H. Electron-microscopic study of the structure of metastable oxides formed in the initial stage of copper oxidation. II. Cu_8O. *Acta Crystallogr., Sect. B: Struct. Sci.* **1984**, *B40*, 560−566.

(62) Bohra, D.; Chaudhry, J. H.; Burdyny, T.; Pidko, E. A.; Smith, W. A. Modeling the electrical double layer to understand the reaction

environment in a CO_2 electrocatalytic system. *Energy Environ. Sci.* **2019**, *12*, 3380−3389.

(63) Zhang, F.; Co, A. C. Direct evidence of local pH change and the role of alkali cation during CO_2 electroreduction in aqueous media. *Angew. Chem., Int. Ed.* **2020**, *59*, 1674−1681.

(64) Zhang, W.; Huang, C.; Xiao, Q.; Yu, L.; Shuai, L.; An, P.; Zhang, J.; Qiu, M.; Ren, Z.; Yu, Y. Atypical oxygen-bearing copper boosts ethylene selectivity toward electrocatalytic CO_2 reduction. *J. Am. Chem. Soc.* **2020**, *142*, 11417−11427.

(65) Bai, H.; et al. Controllable CO adsorption determines ethylene and methane productions from CO_2 electroreduction. *Sci. Bull.* **2020**, DOI: 10.1016/j.scib.2020.06.023.

(66) Yu, J.; Namba, Y. Atomic surface roughness. *Appl. Phys. Lett.* **1998**, *73*, 3607−3609.

(67) Xu, H.; et al. Highly selective electrocatalytic CO_2 reduction to ethanol by metallic clusters dynamically formed from atomically dispersed copper. *Nat. Energy* **2020**, *5*, 623−632.

(68) Jiao, J.; et al. Copper atom-pair catalyst anchored on alloy nanowires for selective and efficient electrochemical reduction of CO_2. *Nat. Chem.* **2019**, *11*, 222−228.

(69) Calle-Vallejo, F.; Koper, M. T. M. Theoretical considerations on the electroreduction of CO to C_2 species on Cu(100) electrodes. *Angew. Chem., Int. Ed.* **2013**, *52*, 7282−7285.

(70) Jiang, K.; Sandberg, R. B.; Akey, A. J.; Liu, X.; Bell, D. C.; Nørskov, J. K.; Chan, K.; Wang, H. Metal ion cycling of Cu foil for selective C−C coupling in electrochemical CO_2 reduction. *Nat. Catal.* **2018**, *1*, 111−119.

(71) Dattila, F. *Glyoxylate-like configurations: (O_{ss})OCCO, sites 1−9.* DOI: 10.19061/iochem-bd-1-165, 2020 (accessed 2020-07-24).

(72) Muchowska, K. B.; Varma, S. J.; Moran, J. Synthesis and breakdown of universal metabolic precursors promoted by iron. *Nature* **2019**, *569*, 104−107.

(73) Handoko, A. D.; Wei, F.; Jenndy; Yeo, B. S.; Seh, Z. W. Understanding heterogeneous electrocatalytic carbon dioxide reduction through operando techniques. *Nat. Catal.* **2018**, *1*, 922−934.

(74) Katayama, Y.; Nattino, F.; Giordano, L.; Hwang, J.; Rao, R. R.; Andreussi, O.; Marzari, N.; Shao-Horn, Y. An *in Situ* surface-enhanced infrared absorption spectroscopy study of electrochemical CO_2 reduction: Selectivity dependence on surface C-bound and O-bound reaction intermediates. *J. Phys. Chem. C* **2019**, *123*, 5951−5963.

(75) Verdaguer-Casadevall, A.; Li, C. W.; Johansson, T. P.; Scott, S. B.; McKeown, J. T.; Kumar, M.; Stephens, I. E.; Kanan, M. W.; Chorkendorff, I. Probing the active surface sites for CO reduction on oxide-derived copper electrocatalysts. *J. Am. Chem. Soc.* **2015**, *137*, 9808−9811.

(76) Álvarez-Moreno, M.; de Graaf, C.; López, N.; Maseras, F.; Poblet, J.; Bo, C. Managing the computational chemistry big data problem: The ioChem-BD Platform. *J. Chem. Inf. Model.* **2015**, *55*, 95−103.